J. Mech. Phys. Solids 153 (2021) 104481

Contents lists available at ScienceDirect

Journal of the Mechanics and Physics of Solids

journal homepage: www.elsevier.com/locate/jmps

Physics-driven machine learning model on temperature and time-dependent deformation in lithium metal and its finite element implementation

Jici Wen [a,c], Qingrong Zou [b], Yujie Wei [a,c,*]

[a] State Key Laboratory of Nonlinear Mechanics (LNM), Institute of Mechanics, Chinese Academy of Sciences, Beijing 100190, China
[b] School of Applied Science, Beijing Information Science and Technology University, Beijing 100192, China
[c] School of Engineering Sciences, University of Chinese Academy of Sciences, Beijing 100049, China

ARTICLE INFO

Keywords:
Physics-driven machine learning
Lithium-metal anode
Creep
Finite-element analysis
Constitutive model

ABSTRACT

Precise understanding on the temperature and time-dependent deformation in lithium-metal anode is of compelling need for durable service of Li-based batteries. Due to both temporal and spatial intertwined thermal agitations and the scarcity of experiments, faithful deformation map of Li-metal covering a broad range of service condition is still lacking. Here we design a physics-driven machine learning (PD-ML) algorithm to map the temperature, stress and rate-dependent deformation in Li-metal. We demonstrate that the PD-ML model, fed with limited experimental results, can predict the mechanical response of Li-metal in a wide span of temperature and deformation rate, and help to realize a deformation map of Li-metal with high fidelity. A finite element (FE) procedure based on the PD-ML constitutive model is then developed. The integration of PD-ML with FE procedure inherits the power of FE analysis and the accuracy originated from PD-ML in describing temperature, stress and rate-dependent mechanical response of Li-metal. The method introduced here paves a new way for constitutive modelling to capture the complex deformation in solids involving multi-field and multiscale mechanics.

1. Introduction

When cataloguing deformation mechanisms and formulate physically sound and faithful constitutive laws for temperature and rate-sensitive deformation in solids, we ought to have deep understandings about the underlying kinetics and thermodynamics of deformation processes occurring in a huge span of spatial and temporal scales (Argon, 1975; Frost and Ashby, 1982; Meyers et al., 1999; Huang et al., 2018). The lack of systematic experimental data at different temperature, stress, and strain rate often leads to an incomplete understanding about the underlying multi-scale deformation, and consequentially render difficulties for the development of predictive constitutive models with high fidelity. The plasticity and creep deformation in solids, for example, are intertwined with each other and are in general a function of temperature, stress and deformation rate (Johnson and Cook, 1985). A highly predictive constitutive model, which may be contingent on limited experimental observations on the mechanical responses at different temperature and strain rate, is of compelling need for a variety of materials in engineering practice.

Li-metal is such a typical example where temperature, stress and deformation rate are involved during its engineering service.

* Corresponding author.
E-mail address: yujie_wei@lnm.imech.ac.cn (Y. Wei).

https://doi.org/10.1016/j.jmps.2021.104481
Received 25 February 2021; Received in revised form 29 April 2021; Accepted 30 April 2021
Available online 6 May 2021

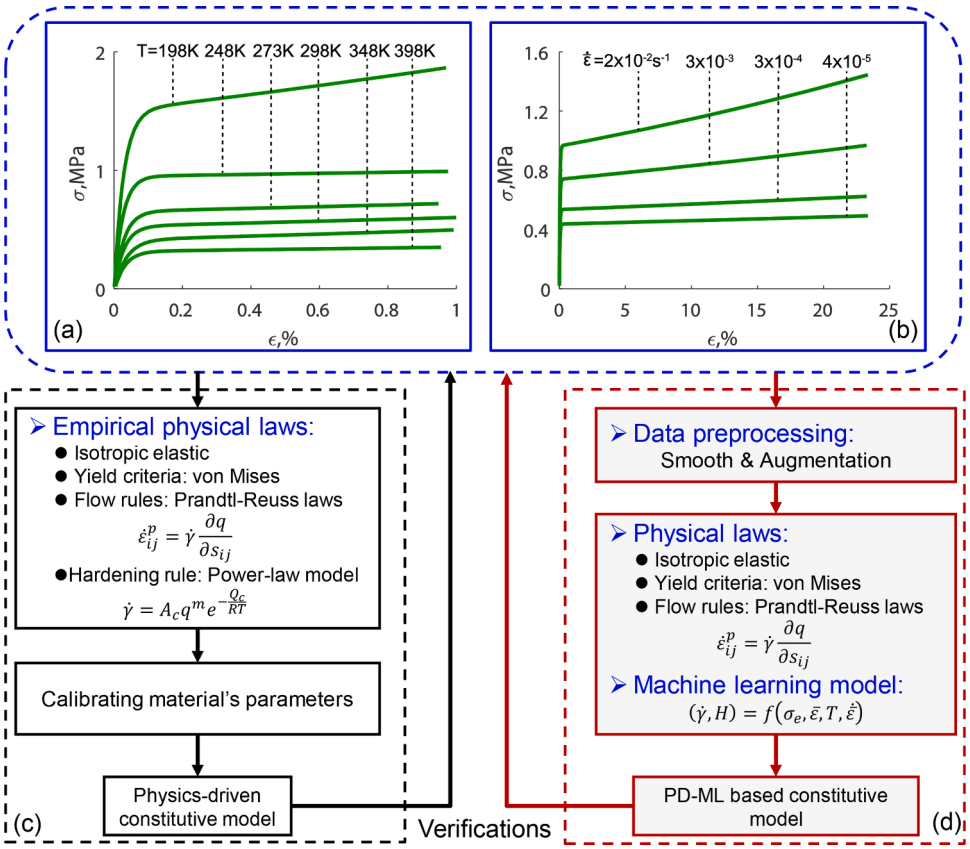

Fig. 1. The conventional vs the PD-ML based constitutive modelling for Li-metal. (a) Stress-strain curves at different temperature and at a constant strain rate $3 \times 10^{-5}/s$, and (b) those at different strain rate at a constant temperature 298 K (experimental data from LePage et al., 2019, replotted). (c) and (d), modelling strategies: (c) A conventional method with explicit formula for plastic flow as a function of stress and temperature. (d) The PD-ML approach, where plastic flow is learned from the numerical algorithm.

Because of its highest theoretical specific capacity (3860 mAh/g), lowest density, and most negative potential (about -3.04 V) (Lin et al., 2017; Wood et al., 2017), Li-metal as the preferred anode is used in many new types of battery including the Li-S battery, the Li-Air battery, and the solid-state battery. However, Li-metal anode gives rise to a series of problems in Li-metal batteries (LMBs), including interfacial contact and resistance (Zhang et al., 2020; Chen et al., 2021), dendrite growth (Xu et al., 2014; Porz et al., 2017; Barai et al., 2017; Wang et al., 2020), mossy and dead Li (Chen et al., 2017), and so on. It is now well known that plastic and creep properties of Li-metal anode have great impact on the performance of the solid-state LMBs by influencing the pressure-dependent interfacial contact and resistance (Krauskopf et al., 2019). Mechanical failures of the Li-metal anode also degrade the electrochemical performance of LMBs (Kozen et al., 2017).

Many related investigations have been done to shed light on the reliability of Li-metal anode due to plasticity and creep at different temperature and strain rate. Wang et al. measured the elastic-visco-plastic mechanical properties of Li-metal by nanoindentation tests (Wang and Cheng, 2017; Herbert, et al., 2018a; 2018b). Masias et al. (2019) characterized stress-strain response and creep behavior of Li-metal in tension and compression. Xu et al. (2017) and Fincher et al. (2020) explored the influence of size and strain-rate on plasticity of Li-metal. Its dependence on both strain rate and temperature was further investigated comprehensively by LePage et al. (2019). Narayan and Anand (2018) formulated a large deformation isotropic elastic–viscoplastic constitutive model for Li-metal. Those experimental investigations and modelling deepen our understanding on the mechanical response of Li-metal anode in variant conditions. There however remain challenges to construct a complete deformation map of Li-metal subject to different temperature and strain rate, or creep at different stress and temperature.

Recent rapid development of the ML method in engineering problems where patterns or scientific principles may be extracted from big data or from strong nonlinear problems. For example, ML method, fed with data from experiments, can be adopted to describe the constitutive behavior of materials. Mozaffar et al. (2019) and Gorji et al. (2020) offers an effective method to predict path-dependent plasticity through deep learning. ML has also been used for new material design (Shi et al., 2019; Bessa et al., 2017; Curtarolo et al., 2013), structural optimization (Liu et al., 2020), property prediction (Kozuch et al., 2018; Hsu et al., 2020), multiscale modeling (Karapiperis et al., 2021), and its development and applications in special domains are rapidly growing (Li et al., 2018).

In the paper, we introduce a new, robust, and accurate constitutive model by combining physical laws with orchestrated ML algorithm for temperature-, stress-, and rate-dependent deformation in Li-metal. We organize the paper as follows. In Section 2, the PD-

Table 1
The material parameters of Li-metal, from (Krauskopf et al., 2019; LePage et al., 2019).

E (MPa)	ν	$\dot{\gamma}_0\ s^{-1}$	σ_0 (MPa)	m	Q_c (kJ · mol^{-1})	$RJ/$(mol · K)
6200	0.401	3.06×10^4	1.0	6.6	37.0	8.314

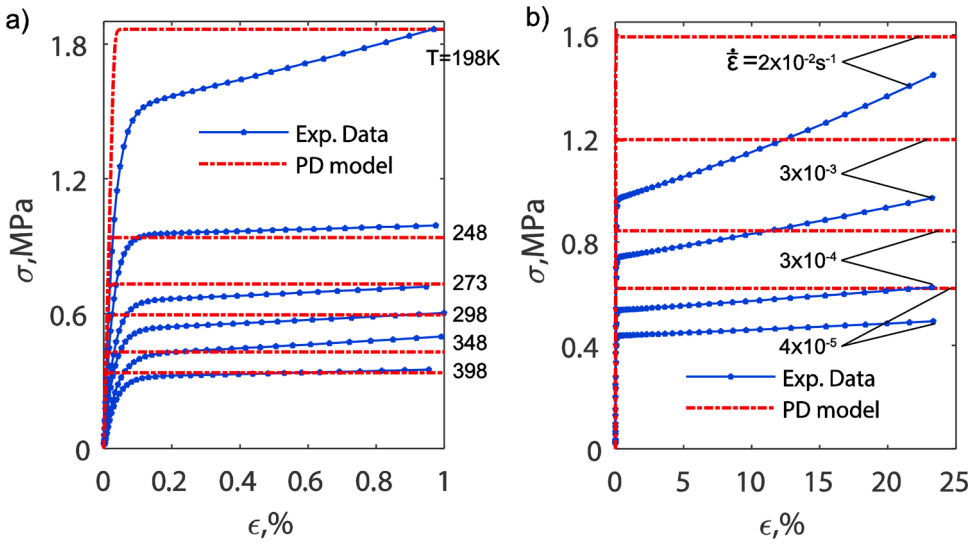

Fig. 2. Predictability of the conventional model on the $\sigma-\varepsilon$ response of Li-metal under uniaxial tension. (a) The temperature dependence of $\sigma-\varepsilon$ curves at a constant strain rate $\dot{\varepsilon}=3\times10^{-5}/s$, predictions from the conventional model vs. experiments; (b) Rate effects predicted by the conventional model vs. experiments (T = 298 K).

ML model of Li-metal and its numerical algorithm is introduced. In Section 3, we verify the PD-ML model using experimental results and demonstrate its robustness and accuracy. The PD-ML model is then implemented in the commercial FE package ABAQUS (DS Simulia Corp., 2020) as a user-material subroutine (UMAT), and we further explore the applicability of the PD-ML-FEM algorithm for the deformation of Li-metal in Section 4. We conclude in Section 5 with final remarks and discussions.

2. Physics-driven machine learning algorithm

To construct a faithful constitutive model which satisfying the thermodynamic principles and conservation laws, we often need systematic experimental observations to shed light on the underlying deformation process, to reveal the dependence of all variates, to calibrate unknown constants in the equations, and to validate the predictability of the constitutive model. As shown in Fig. 1, with experimental data given in Figs. 1a and b (LePage et al., 2019), we may either adopt a conventional modelling approach or a PD-ML algorithm, as to be explained next.

For the conventional constitutive model on Li-metal, the dependence of plastic flow on stress and temperature is known as a prior. As seen in Fig. 1a, the stress-strain curves of the bulk Li-metal under uniaxial tension exhibit typical elastic-plastic response of polycrystalline metals, yielding and irrecoverable plastic deformation after the initial elasticity. The isotropic linear elastic response is characterized by a Young's modulus E and a Poisson's ratio ν. After yielding, the Li-metal may sustain a large amount of plastic deformation with tensile failure-strain up to 30% (Hull and Rosenberg, 1959). Li-metal has a low melting temperature (453 K) and low activation energy for self-diffusion (50 kJ · mol^{-1}) (Messer and Noack, 1975; Hao et al., 2018). The dominant mechanism accounting for the plasticity is due to the coble creep at its working temperature for electric vehicle batteries, in the range of 233 to 323 K (Chen et al., 2020; Wang et al., 2020; Zhang, 2011). It therefore leads to a highly rate-sensitive deformation, as seen in Fig. 1b.

In the conventional approach, we use the von Mises-based visco-plastic theory with isotropic strain hardening. The Prandtl-Reuss laws is adopted for the plastic flow as

$$\dot{\varepsilon}^p_{ij}=\dot{\gamma}\frac{\partial\overline{\sigma}}{\partial s_{ij}}, \tag{1}$$

where $\dot{\varepsilon}^p_{ij}$ is the plastic strain rate tensor, $\dot{\gamma}$ is the equivalent strain rate, $\overline{\sigma}=\sqrt{\frac{3}{2}s_{ij}s_{ij}}$ is the von Mises stress, $s_{ij}=\sigma_{ij}+p\delta_{ij}$ is the deviatoric part of the Cauchy stress σ_{ij}, and $p=-\frac{1}{3}\sigma_{ij}\delta_{ij}$ is the hydrostatic pressure for δ_{ij} being the Kronecker delta function ($\delta_{ij}=1$ if $i=j$, and 0 if $i\neq j$). The plastic strain rate $\dot{\gamma}$ is characterized by a set of creep constants (LePage et al., 2019; Masias et al., 2019),

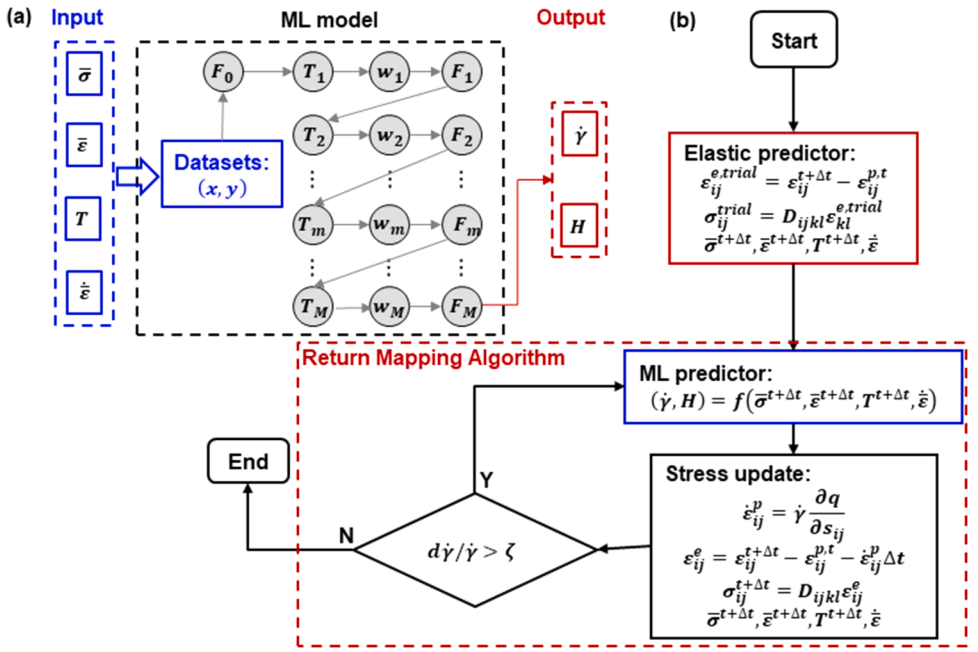

Fig. 3. The integrated ML algorithm with physical assumptions. (a) Diagram to show the input to and the output from the ML model, and (b) the numerical algorithm for the constitutive model integrating PD-ML.

$$\dot{\gamma} = \dot{\gamma}_0 (\bar{\sigma}/\sigma_0)^m e^{\left(-\frac{Q_c}{RT}\right)}, \tag{2}$$

which includes a creep component m, an activation energy Q_c, a kinetic constant $\dot{\gamma}_0$, the corresponding reference stress σ_0, the gas constant R, and the absolute temperature T.

We implemented the conventional constitutive model shown in Fig. 1c in the commercial finite-element (FE) software Abaqus as a user material subroutine (DS Simulia Corp., 2020). With parameters listed in Table 1, we obtain the tensile stress-strain curves at different temperature and a constant strain rate from FE calculations in Fig. 2a, and the rate-sensitivity of the mechanical response at a given temperature in Fig. 2b. We can see that the conventional power-law model fails to capture the stress hardening and rate-dependence, which, in principle, reflects the weakness of the model (see Eq. 2) in predicting the stress- and temperature-dependent creep rate. It is noted that improvements to the fitting may be possible through the use of more complicated hardening or by using series solution in the power-law creep. The hardening behavior in Li-metal may be included in the power-law creep by formulating σ_y as $\sigma_y = H(T,\dot{\gamma})\bar{\varepsilon}_p^{n(T,\dot{\gamma})}$, where $H(T,\dot{\gamma})$ and $n(T,\dot{\gamma})$ are respectively the strain hardening modulus and exponent. We may alternatively employ series solutions and write the collective power-law flow rate as $\dot{\gamma} = \sum_{i=1}^{M} \dot{\gamma}_{0,i} \left[\frac{\bar{\sigma}}{\sigma_{0,i}}\right]^{m_i}$, where $(\dot{\gamma}_{0,i}, \sigma_{0,i}, m_i,\ i = 1, \ldots, M)$ are variables to be fitted. Nevertheless, determining these parameters are not trivial. In most circumstances, they are not universal and cannot be quantified uniquely. It becomes worse when experimental data is limited.

To better capture the stress- and temperature-dependent plastic flow, we adopt a PD-ML model to supplant the regular power-law flow in Li-metal, as shown in Fig. 3. As the prior physical knowledge (physics driven, PD), those variables $(\bar{\sigma},\ \bar{\varepsilon}, T, \dot{\bar{\varepsilon}})$, acquired from experimental data, are selected as inputs, where $\dot{\bar{\varepsilon}} = \sqrt{\frac{2}{3}\dot{\varepsilon}_{ij}\dot{\varepsilon}_{ij}}$ is the equivalent strain rate and $\bar{\varepsilon} = \int \dot{\bar{\varepsilon}} dt$ is the equivalent strain, and $\dot{\varepsilon}_{ij}$ and t are the strain rate tensor and time, respectively. The outputs include the plastic strain rate $\dot{\gamma}$ and the strain hardening H ($H = \frac{\partial \bar{\sigma}}{\partial \gamma}$). In brief, the learning algorithm is a function to realize the following mapping through machine learning (ML)

$$(\dot{\gamma}, H) = f(\bar{\sigma},\ \bar{\varepsilon}, T, \dot{\bar{\varepsilon}}), \tag{3}$$

Note that $f(\cdot)$, in contrast to have an explicit expression in terms of its variables, represents a black-box function embedded in the PD-ML algorithm. The learned $\dot{\gamma}$ will be used for stress update, and H is needed for the consistence condition on the yield surface. The plastic flow in Li-metal (see Eq. 3) is multi-factor influenced and highly nonlinear. Given there are only a small amount of experimental data, we choose the tree-based ML algorithm over other ML algorithms (e.g., the support vector machine, the tree-based ML algorithm, and the artificial neural network). A complete description about the learning algorithm is supplied in Appendix A.

Fig. 3b gives the iterative process to ensure convergence. The numerical procedure composes of standard elastic predictor and visco-plastic updating. From time t to $t + \Delta t$, an initial predictor, by assuming the incremental strain being elastic, we obtain a trial

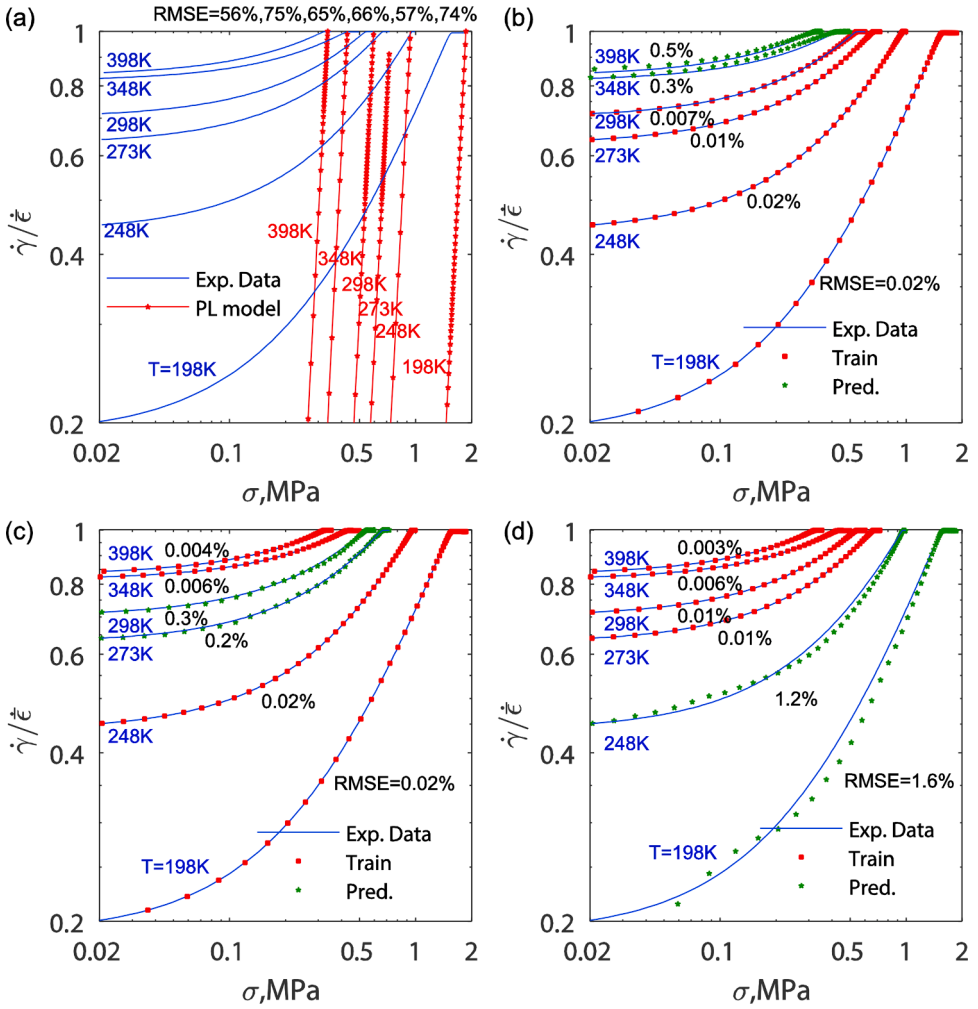

Fig. 4. Predictability of the conventional model and the PD-ML model on $\dot{\gamma}/\dot{\bar{\varepsilon}} - \sigma$ relation at different temperatures. (a) Traditional model vs. experiments. (b) to (d) Trained and predicted results from PD-ML model vs experiments: (b) The predicted curves at temperatures (348 and 398 K) higher than those of the trained ones. (c) The predicted curves at temperatures (273 and 298 K) within the trained temperature range. (d) The predicted curves at temperatures (198 and 248 K) lower than those of the trained ones.

elastic strain $\varepsilon_{ij}^{e,trial}$ at current time step,

$$\varepsilon_{ij}^{e,trial} = \varepsilon_{ij}^{t+\Delta t} - \varepsilon_{ij}^{p,t} \tag{4a}$$

and update the trial stress σ_{ij}^{trial} as

$$\sigma_{ij}^{trial} = D_{ijkl}\varepsilon_{kl}^{e,trial} \tag{4b}$$

where D_{ijkl} is the four order elastic constant tensor. Once visco-plastic deformation involves, the implicit return-mapping PD-ML algorithm takes over to update $\dot{\gamma}$ and H. With σ_{ij}^{trial} being the first guess, we proceed with an iterative process by taking the current von Mises stress $\bar{\sigma}^{t+\Delta t}$, equivalent strain $\bar{\varepsilon}^{t+\Delta t}$, temperature $T^{t+\Delta t}$, and equivalent strain rate $\dot{\bar{\varepsilon}}$ as inputs to the PD-ML and update $\dot{\gamma}$ and H, see Fig. 3b for illustration. The standard associative flow rule in Eq. (1) is then used to update the plastic strain rate $\dot{\varepsilon}_{ij}^{p}$. Sequentially, we may write the current elastic strain and stress tensor as

$$\varepsilon_{ij}^{e} = \varepsilon_{ij}^{t+\Delta t} - \varepsilon_{ij}^{p,t} - \dot{\varepsilon}_{ij}^{p}\Delta t \tag{5a}$$

and

$$\sigma_{ij}^{t+\Delta t} = D_{ijkl}\varepsilon_{ij}^{e} \tag{5b}$$

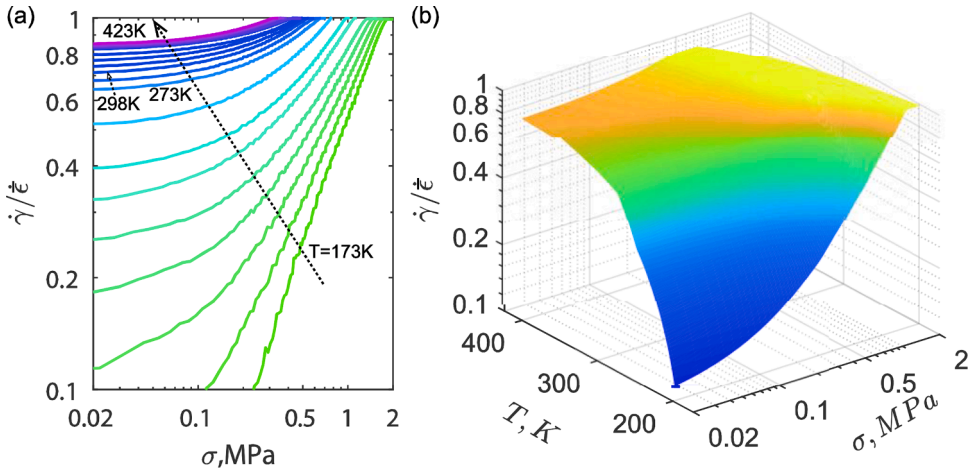

Fig. 5. Deformation map of Li-metal. (a)$\dot{\gamma}/\dot{\bar{\varepsilon}}$ vs. σ for a wide range of temperatures. (b) A three-dimensional diagram to show the temperature T, stress σ, and plastic flow $\dot{\gamma}/\dot{\bar{\varepsilon}}$ relationship. It covers a wide temperature span from 173 to 423 K.

respectively. The iteration continues till $\dot{\gamma}$ satisfying the following criterion. The difference of $\dot{\gamma}$ between this step and the previous one, $d\dot{\gamma}$, is infinitesimal, i.e., $d\dot{\gamma}/\dot{\gamma} < \zeta$ for ζ being a small tolerance. With known $d\dot{\gamma}$, we may proceed to update strains at time $t + \Delta t$, $\varepsilon_{ij}^{p,t+\Delta t} = \varepsilon_{ij}^{p,t} + \dot{\varepsilon}_{ij}^{p}\Delta t$, $\varepsilon_{ij}^{e} = \varepsilon_{ij}^{t+\Delta t} - \varepsilon_{ij}^{p,t+\Delta t}$, and $\sigma_{ij}^{t+\Delta t}$ before the next time increment.

3. Results with the PD-ML model

We now apply both the conventional model and the PD-ML model to the viscoplastic deformation of Li-metal, and demonstrate their predictability in comparison with available experimental data. Both temperature and strain rate factors are taken into account in the two types of models.

3.1. Temperature-dependence

As seen in Fig. 4, we first show the normalized plastic strain rate $\dot{\gamma}/\dot{\bar{\varepsilon}}$ as a function of stress σ from experiments at six temperatures (Fig. 4a). It is seen that $\dot{\gamma}$ increases slowly under low stress, followed by a rapid ascending at intermediate to high stress. At the late stage, plastic strain $\dot{\gamma}$ dominates and approaches to the applied strain rate $\dot{\bar{\varepsilon}}$, i.e., $\dot{\gamma}/\dot{\bar{\varepsilon}} \to 1$. There is a strong nonlinear dependence of $\dot{\gamma}$ and σ on temperature. The traditional power law model with Eq. (2) assumes intrinsically a linear relationship in the log-log scale of $\dot{\gamma}$ vs. σ (curves with asterisks in Fig. 4a, and the maximum root mean square error (RMSE) is about 75%. Here RMSE $= \sqrt{\frac{\sum_{i=1}^{N}(r_i - \widehat{r}_i)^2}{N}}$, for r $= \dot{\gamma}/\dot{\bar{\varepsilon}}$and $\widehat{r}$ being the predicted value and the experimental value, respectively, and N the number of data points. It fails to capture the real experimental observations.

For verifying the predictability of the PD-ML model at a series of stress and temperature range, we next divide the experimental data into two datasets: curves at four temperatures out of six are adopted for training, and the rest two are used for prediction. Here three different types of sampling are used, and the corresponding errors at different temperature are shown in Figs. 4b to d. In Fig. 4b, we choose the curves at 348 K and 398 K for prediction, which are higher than those four temperatures used for training. The extrapolated prediction leads to a prediction error about 0.3% at 348 K and 0.5% at 398 K. While the RSME error is significantly higher than those of the training dataset (in comparison with experimental data), the absolute errors are rather small, indicating the excellent capability for extrapolating beyond the higher end of temperature. When we choose to predict the $\dot{\gamma}$-σ curves at temperatures falling within those of the training dataset as shown in Fig. 4c, the predicted curves at 273 K and 298 K match very well with experimental results, and the error are about 0.3% and 0.2%, respectively. We show in Fig. 4d the predictions at temperatures lower than those of the four in the training dataset. Corresponding errors are 1.2% at 248 K and 1.6% at 198 K. Although the predictions from the PD-ML model exhibit different level of errors based on the selection of training dataset and prediction dataset, the three characteristic sampling methods demonstrate high fidelity of the PD-ML model to capture existing experimental data. We also explored the sensitivity of the training dataset on the predictability of the learning algorithm for $\dot{\gamma}/\dot{\bar{\varepsilon}} - \sigma$ relationship. As shown in Fig. B1 (see Appendix B), the accuracy increases as the training dataset increases, and a minimum of stress-strain curves at three different temperature should be given. Furthermore, the model exhibits very good accuracy when generalizing to temperatures beyond the range of the training dataset, which is essential for deformation mapping as experimental data are insufficient to cover a wide range of temperature, stress and strain rate, respectively or in combination. We then used all available data at six temperatures for training, and construct the deformation map of Li-metal in Fig. 5a, where the relationship of $\dot{\gamma}/\dot{\bar{\varepsilon}}$ and σ at a wide range of temperatures is presented.

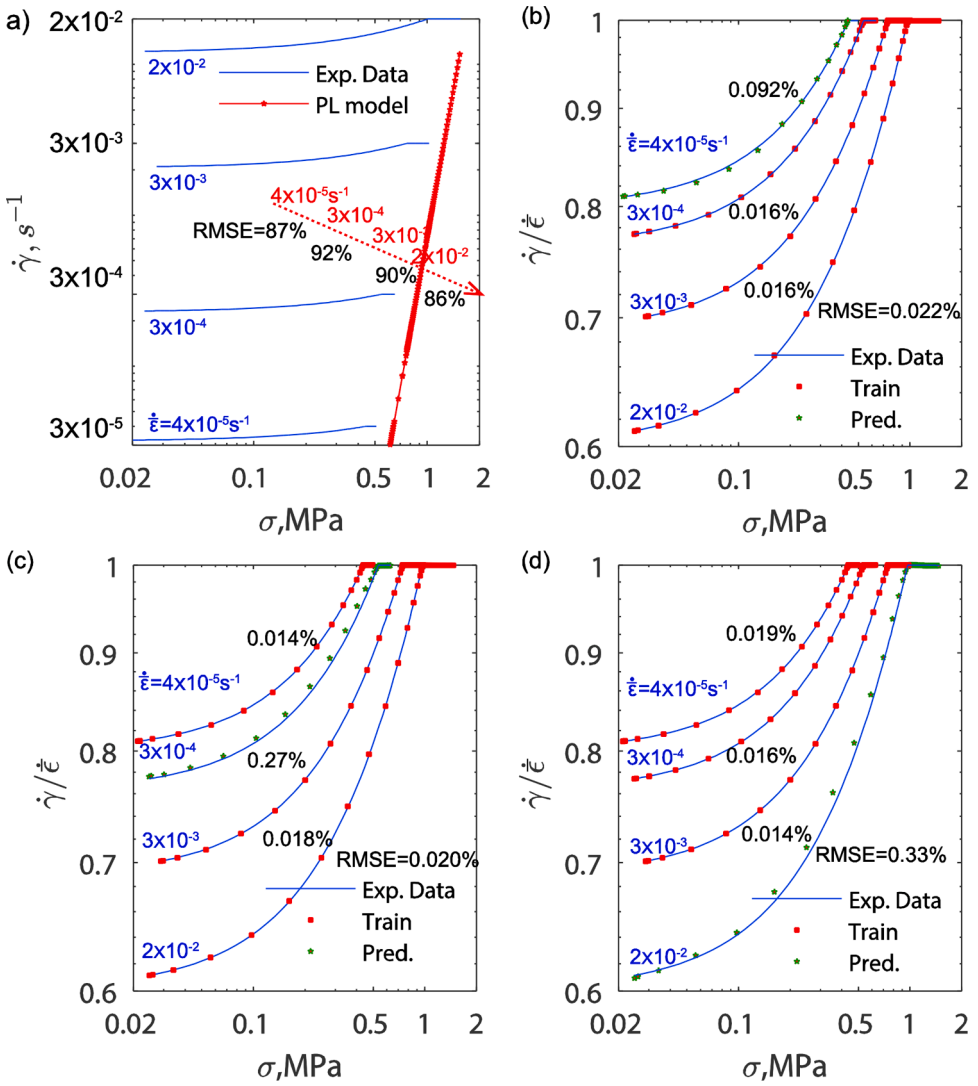

Fig. 6. Predictability of the conventional model and the PD-ML model on $\dot{\gamma}/\dot{\bar{\varepsilon}} - \sigma$ relationship at different strain rate. (a) Traditional model vs. experiments. (b) to (d) Trained and predicted results from PD-ML model vs experiments: (b) The predicted curves at strain rate ($4 \times 10^{-5}/s$) lower than those of the trained ones. (c) The predicted curves at strain rate ($3 \times 10^{-4}/s$) within the trained rate range. (d) The predicted curves at $2 \times 10^{-2}/s$, which is higher than those of the trained ones.

Also, a three dimensional diagram to show the temperature T, stress σ, and plastic flow $\dot{\gamma}/\dot{\bar{\varepsilon}}$ is seen in Fig. 5b. The deformation map covers a wide temperature span from 173 K to 423 K, which covers most environmental conditions for Li-metal in engineering service.

3.2. Strain-rate sensitivity

Li-metal's deformation is closely subject to the time during charging and discharging process, and may be subject to dynamic loading. Rate sensitive deformation in Li-metal plays an important role on the performance of LMBs. The conventional visco-plastic constitutive model fails to capture the influence of strain rate. In the σ - $\dot{\gamma}$ curves, the maximum RMSE is about 92%, as shown in Fig. 6a.

By adding the applied strain rate $\dot{\bar{\varepsilon}}$ as an input to the PD-ML model (see Eq. 3), we may learn from the $\dot{\gamma}/\dot{\bar{\varepsilon}} - \sigma$ curves at certain loading rates and therefore predict the curves at other rates. Following the learning-prediction method we adopted for temperature dependence, we take the $\dot{\gamma}/\dot{\bar{\varepsilon}} - \sigma$ curves at three different strain rate as training dataset, and the rest for prediction. The strain rate of the experimental curve for prediction may be higher than, within, or lower than those rates in the training dataset. The learning vs experimental curves and the predicted one for these three sampling method are also shown in Figs. 6b to d, respectively. In Fig. 6b, we choose the curve at the strain rate $4 \times 10^{-5}/s$ for prediction. The extrapolated prediction has an RSME error about 0.092%. When we choose to predict the $\dot{\gamma}$-σ curves at the strain rate $3 \times 10^{-4}/s$ which is within those of the training dataset (Fig. 6c), the error is about 0.27%. We show in Fig. 6d the predictions at strain rate higher than those of the three in the training set. The corresponding error is

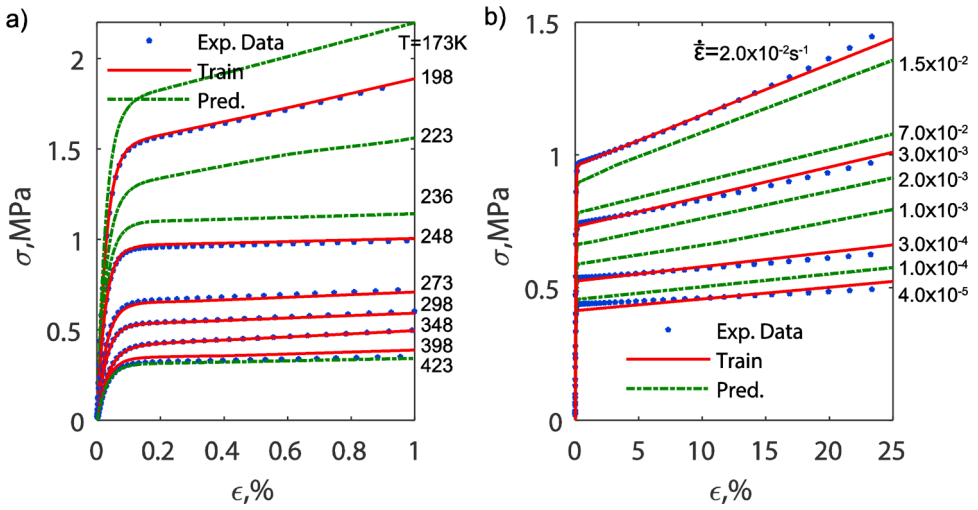

Fig. 7. Predictability of the PD-ML model on $\sigma - \varepsilon$ curves under uniaxial tension. (a) Training and prediction results from PD-ML model vs. experiments at different temperature ($\dot{\bar{\varepsilon}} = 3 \times 10^{-5}/s$); (b) Training and prediction from PD-ML model vs. experiments at different strain rate (T = 298 K).

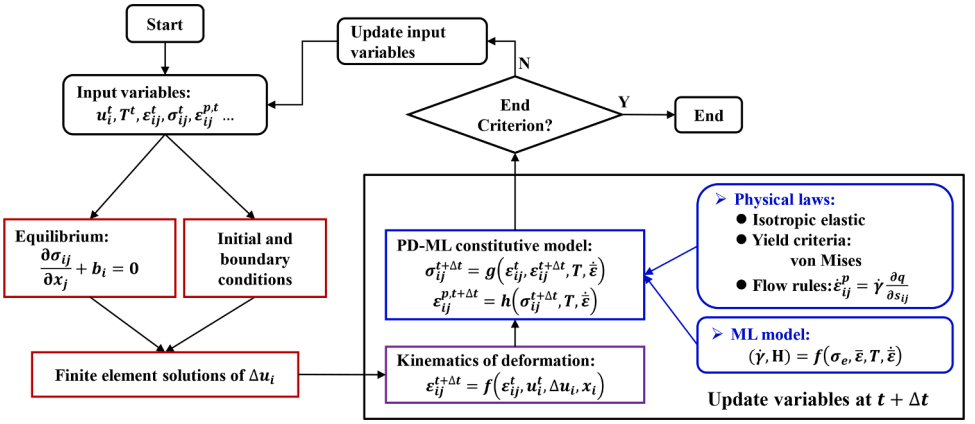

Fig. 8. Schematic diagram to show the integration of physics-driven machine learning based constitutive modelling with finite element procedures.

0.33%. Although the predictions from the PD-ML model exhibit different errors based on the selection of training dataset and prediction dataset, the three characteristic sampling methods demonstrate the high fidelity of the PD-ML model to capture existing experimental data.

3.3. *Temperature and rate-dependent response*

With the stress-strain curves reported by LePage et al. (2019), we can now examine the predictability of the PD-ML model for a variety of temperatures and strain rates. We show in Fig. 7a the $\sigma - \varepsilon$ curves under uniaxial tensile test from both the PD-ML model and experiments at different temperature and at a constant strain rate of $\dot{\bar{\varepsilon}} = 3 \times 10^{-5}/s$. In contrast to the same prediction from the conventional model shown in Fig. 2a, we see that at all temperatures the former performs better to capture not only the nonlinear strain-hardening at small strains, but also the stress plateau at large strains. In Figs. 7b and 2b, predictions on the stress-strain responses at different strain rate and at constant temperature T = 298 K from the PD-ML model and the conventional model are shown, respectively. The conventional model fails to capture the distinct strain hardening at different strain rate; the PD-ML model leads to good agreement with experiment curves for training and those for prediction. Therefore, it is capable of predicting the stress-strain behavior of Li-metal at arbitrary temperatures and at strain rates of engineering interest.

4. Finite-element implementation of the PD-ML model

In Section 3, we have shown that the PD-ML model is more accurate and robust than the conventional constitutive model for

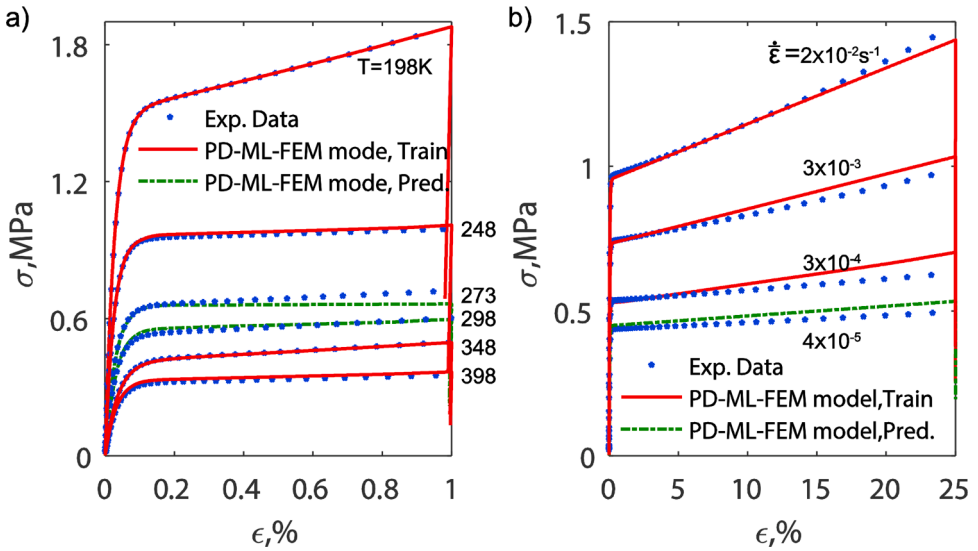

Fig. 9. Predictability verifications of the PD-ML-FEM model on the $\sigma - \varepsilon$ curves under uniaxial tensile testing. (a) Trained and predicted results from PD-ML-FEM model vs. experiments at different temperature ($\dot{\bar{\varepsilon}} = 3 \times 10^{-5}/s$); (b) Training and prediction from PD-ML-FEM model vs. experiments at different strain rate (T = 298 K).

describing the temperature and strain-rate dependent deformation in Li-metal. It is then promising to implement the PD-ML constitutive model in FE procedures, as we do for conventional flow rules (Eq. 2 for example), and using the power of FE method to compute complex boundary-value problems. In Fig. 8, we show a schematic diagram to integrate the PD-ML constitutive modelling with FE procedures.

We illustrate the displacement based incremental PD-ML-FEM model as follows: At time t and material point x_i, input variables ($u_i^t, T, \varepsilon_{ij}^t, \sigma_{ij}^t, \varepsilon_{ij}^{p,t}$ and other inner variables) are given, and the incremental displacements $\Delta u_i = u_i^{t+\Delta t} - u_i^{\Delta t}$ from time t to $t + \Delta t$ are known from the solution of global equilibrium. The current strain $\varepsilon_{ij}^{t+\Delta t}$ is updated. The PD-ML constitutive model is then applied to update the current stress tensor $\sigma_{ij}^{t+\Delta t}$, the current plastic strain $\varepsilon_{ij}^{t+\Delta t,p}$, and related inner variables. With the updated stress status at element level, the equilibrium condition solved by the finite element procedure leads to an updated displacement incremental Δu_i. We show next the application of the implemented PD-ML-FEM model in ABAQUS (DS Simulia Corp., 2020).

In Fig. 9, we examine the predictability of the PD-ML-FEM model on the $\sigma - \varepsilon$ response of Li-metal under uniaxial tension. Here we firstly select the sampling strategy that the temperatures of the predicted curve are falling within those of the training dataset, which has the best predictability for $\dot{\gamma}$-σ curves (RMSE<0.3%), as seen in Fig. 9a. We can see that the trained results from the PD-ML-FEM model agree well with experimental results, in contrast to the conventional power-law constitutive model in Fig. 2a. At a given temperature, the predictability of the PD-ML-FEM model on the strain-rate sensitivity of $\sigma - \varepsilon$ curves is examined and the results is shown in Fig. 9b. Here the curve at the strain rate $4 \times 10^{-5}/s$ is chosen for prediction, and its corresponding predicted error (RMSE) is lower than 0.1%. We can see that both the trained and the predicted results demonstrate the high fidelity of the PD-ML-FEM model to capture existing experimental data, and the model is also capable of generalizing to predict the mechanical response beyond experimental observations.

5. Conclusions

While deformation map is of prominent significance in nearly all engineering materials, constructing a faithful map of a particular material subject to deformation at a wide variety of temperature and strain rate is a grand challenge. The intertwined deformation mechanisms in a huge span of spatial and temporal scale may change their dominance abruptly or gradually in response to temperature and rate variation. In this paper, we focus on the deformation of Li-metal, and develop a PD-ML algorithm to map the temperature, stress and rate-dependent deformation in Li-metal. It has been demonstrated that the PD-ML model, in contrast to conventional models, show great precision enhancements when mapping temperature, stress and rate-dependent deformation of Li-metal. Its predictability in a wide span of temperature and deformation rate is essential to realize a deformation map of Li-metal with high fidelity. The PD-ML constitutive model is then implemented in a commercial finite element software. We demonstrate that a well orchestrated ML algorithm can be adopted to develop constitutive models of high efficacy. In combination with powerful FE procedures, the novel modelling strategy may then be used to simulate complex deformation in systems involving multi-physics process and subject to a variate of boundary conditions. The method can also be conveniently generalized to ubiquitous engineering materials with temperature, stress, strain-rate dependent deformation, and paves a way for the development of data-driven constitutive modelling.

Declaration of Competing Interest

The authors declare that they have no known competing financial interests or personal relationships that could have appeared to influence the work reported in this paper.

Author statement

Wei conceived the research. Wen developed the physics-driven ML model. Wen and Zou carried out data processing and analysis. Wei and Wen write the paper. All authors read and approved the final version.

Acknowledgements

The authors acknowledge supports from the NSFC Basic Science Center for 'Multiscale Problems in Nonlinear Mechanics' (No. 11988102), the National Natural Science Foundation of China (NSFC) (No. 12002343), the Strategic Priority Research Program of the Chinese Academy of Sciences (XDB22020200), and CAS Center for Excellence in Complex System Mechanics, Zou thanks the Scientific Research Foundation Project of Beijing Information Science and Technology University (No. 2025032).

Appendix A. The tree-based learning algorithm

We adopt the tree-based algorithm for regression (Gradient boosting regression), which is composed of multiple regression trees to capture the nonlinear interaction relationship between the features and the target (Natekin and Knoll, 2013; Friedman et al., 2000), and its algorithm structure is summarized in Fig. 3a. We arrive with the dataset $(\boldsymbol{x},\boldsymbol{y})_{i=1}^{N}$, where $\boldsymbol{x}_i = (\overline{\sigma},\ \overline{\varepsilon}, T, \dot{\overline{\varepsilon}})$ and $\boldsymbol{y}_i = (\dot{\gamma}, H)$ refer to the input variables and its corresponding output variables, respectively, and N is the total number of samples. In order to reconstruct the unknown functional dependence between $\boldsymbol{x}$ and $\boldsymbol{y}$ with our estimate $F(\boldsymbol{x})$, the initial model with a constant value is given as

$$F_0(\boldsymbol{x}) = \arg\ \min_{\theta_0} \sum_{i=1}^{N} L(\boldsymbol{y}_i, \boldsymbol{\theta}_0), \tag{A1}$$

which satisfies the loss function minimization. In the paper, the classic squared-error L_2 loss function is used as $L(\boldsymbol{y}_i,\boldsymbol{\theta}) = \frac{1}{2}(\boldsymbol{y}_i - \boldsymbol{\theta})^2$. We set M tree base learners in the model, in which the m-th tree base learner $\boldsymbol{T}_m(\boldsymbol{x}_i,\boldsymbol{\theta}_m)$ is estimated by the gradient descent procedure on the residuals as

$$\boldsymbol{r}_{im} = -\left\{\frac{\partial L[\boldsymbol{y}_i, F(\boldsymbol{x}_i)]}{\partial F(\boldsymbol{x}_i)}\right\}_{F(\boldsymbol{x}_i)=F_{m-1}(\boldsymbol{x}_i)}, for\ i = 1, 2\ldots N, \tag{A2}$$

and the parameters of the m-th tree base learner, $\boldsymbol{\theta}_m$, are given as

$$\boldsymbol{\theta}_m = \arg\ \min_{\boldsymbol{\theta}} \sum_{i=1}^{N} L[\boldsymbol{r}_{im}, \boldsymbol{T}(\boldsymbol{x}_i, \boldsymbol{\theta})], \tag{A3}$$

and the multiplier $\boldsymbol{w}_m$ are

$$\boldsymbol{w}_m = \arg\ \min_{w} \sum_{i=1}^{N} L[\boldsymbol{y}_i, F_{m-1}(\boldsymbol{x}_i) + \boldsymbol{w}\boldsymbol{T}(\boldsymbol{x}_i, \boldsymbol{\theta}_m)]. \tag{A4}$$

And finally, we update the model as

$$F_m(\boldsymbol{x}) = F_{m-1}(\boldsymbol{x}) + \boldsymbol{w}_m \boldsymbol{T}(\boldsymbol{x}_i, \boldsymbol{\theta}_m). \tag{A5}$$

In this tree-based learning algorithm, the number of trees M, the maximum depth of individual regression estimators and the minimum number of samples in a node for controlling over-fitting, and the learning rate for the impact of each tree on the final outcome, are tuned to minimize the L_2 loss function. Those hyper-parameters are optimized by using the grid-search strategy, and the experimental data are splitting into a training dataset and a prediction dataset, as we introduced in Section 3.

Appendix B. The sensitivity of training dataset on the predictability of the learning algorithm for the visco-plastic response in Li-metal

Fig. B1

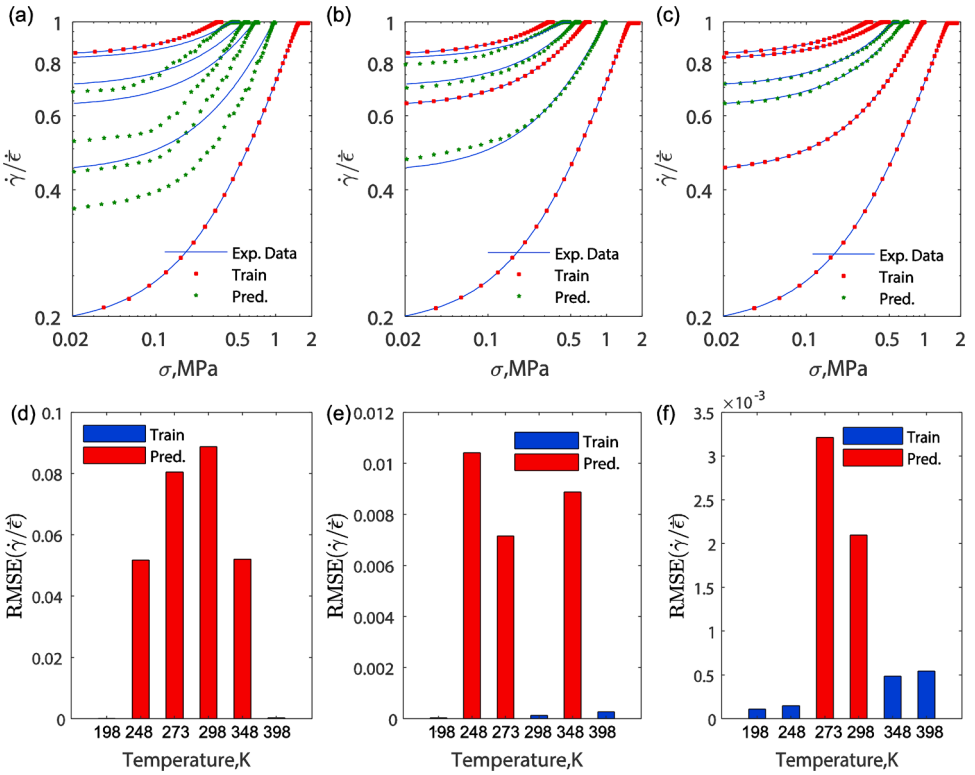

Fig. B1. The sensitivity of training dataset on the predictability of the PD-ML model on $\dot{\gamma}/\dot{\bar{\varepsilon}} - \sigma$ relation at different temperature. (a) to (c) Trained and predicted results from PD-ML model vs experiments, and (d) to (f) the corresponding RMSE errors at different temperature.

References

Argon, A.S., 1975. Constitutive Equations in Plasticity. MIT press, Cambridge.

Barai, P., Higa, K., Srinivasan, V., 2017. Lithium dendrite growth mechanisms in polymer electrolytes and prevention strategies. Phys. Chem. Chem. Phys. 19 (31), 20493–20505.

Bessa, M.A., Bostanabad, R., Liu, Z., Hu, A., Apley, D.W., Brinson, C., Chen, W., Liu, W.K., 2017. A framework for data-driven analysis of materials under uncertainty: countering the curse of dimensionality. Comput. Methods Appl. Mech. Eng. 320, 633–667.

Chen, K.H., Wood, K.N., Kazyak, E., LePage, W.S., Davis, A.L., Sanchez, A.J., Dasgupta, N.P., 2017. Dead lithium: mass transport effects on voltage, capacity, and failure of lithium metal anodes. J. Mater. Chem. A Mater. 5 (23), 11671–11681.

Chen, C., Jiang, M., Zhou, T., Raijmakers, L., Vezhlev, E., Wu, B., Schülli, T.U., Danilov, D.L., Wei, Y., Eichel, R.A., Notten, P.H.L., 2021. Interface aspects in all-solid-state li-based batteries reviewed. Adv. Energy Mater. 11 (13), 2003939.

Chen, Y., Wang, Z., Li, X., Yao, X., Wang, C., Li, Y., Li, J., 2020. Li metal deposition and stripping in a solid-state battery via Coble creep. Nature 578 (7794), 251–255.

Curtarolo, S., Hart, G.L., Nardelli, M.B., Mingo, N., Sanvito, S., Levy, O., 2013. The high-throughput highway to computational materials design. Nat. Mater. 12 (3), 191–201.

DS Simulia Corp., 2020. ABAQUS/CAE User's Guide. Dassault Systèmes (DS) Simulia Corp., RI, USA.

Fincher, C.D., Ojeda, D., Zhang, Y., Pharr, G.M., Pharr, M., 2020. Mechanical properties of metallic lithium: from nano to bulk scales. Acta Mater. 186, 215–222.

Friedman, J., Hastie, T., Tibshirani, R., 2000. Additive logistic regression: a statistical view of boosting (with discussion and a rejoinder by the authors). Ann. Stat. 28 (2), 337–407.

Frost, H.J., Ashby, M.F., 1982. Deformation Mechanism Maps: the Plasticity and Creep of Metals and Ceramics. Pergamon press.

Gorji, M.B., Mozaffar, M., Heidenreich, J.N., Cao, J., Mohr, D., 2020. On the potential of recurrent neural networks for modeling path dependent plasticity. J. Mech. Phys. Solids 143, 103972.

Hao, F., Verma, A., Mukherjee, P.P., 2018. Mesoscale complexations in lithium electrodeposition. ACS Appl. Mater. Interfaces 10 (31), 26320–26327.

Herbert, E.G., Hackney, S.A., Dudney, N.J., Phani, P.S., 2018a. Nanoindentation of high-purity vapor deposited lithium films: the elastic modulus. J. Mater. Res. 33 (10), 1335–1346.

Herbert, E.G., Hackney, S.A., Thole, V., Dudney, N.J., Phani, P.S., 2018b. Nanoindentation of high-purity vapor deposited lithium films: a mechanistic rationalization of diffusion-mediated flow. J. Mater. Res. 33 (10), 1347–1360.

Hsu, Y.C., Yu, C.H., Buehler, M.J., 2020. Using deep learning to predict fracture patterns in crystalline solids. Matter 3 (1), 197–211.

Huang, W., Li, J., Edwards, P., 2018. Mesoscience: exploring the common principle at mesoscales. Natl. Sci. Rev. 5 (3), 321–326.

Hull, D., Rosenberg, H.M., 1959. The deformation of lithium, sodium and potassium at low temperatures: tensile and resistivity experiments. Philos. Mag. 4 (39), 303–315.

Johnson, G.R., Cook, W.H., 1985. Fracture characteristics of three metals subjected to various strains, strain rates, temperatures and pressures. Eng. Fract. Mech. 21 (1), 31–48.

Karapiperis, K., Stainier, L., Ortiz, M., Andrade, J.E., 2021. Data-Driven multiscale modeling in mechanics. J. Mech. Phys. Solids 147, 104239.

Kozen, A.C., Lin, C.F., Zhao, O., Lee, S.B., Rubloff, G.W., Noked, M., 2017. Stabilization of lithium metal anodes by hybrid artificial solid electrolyte interphase. Chem. Mater. 29 (15), 6298–6307.

Kozuch, D.J., Stillinger, F.H., Debenedetti, P.G., 2018. Combined molecular dynamics and neural network method for predicting protein antifreeze activity. Proc. Natl. Acad. Sci. 115 (52), 13252–13257.

Krauskopf, T., Hartmann, H., Zeier, W.G., Janek, J., 2019. Toward a fundamental understanding of the lithium metal anode in solid-state batteries—an electrochemo-mechanical study on the garnet-type solid electrolyte Li6.25Al0.25La3Zr2O12. ACS Appl. Mater. Interfaces 11 (15), 14463–14477.
LePage, W.S., Chen, Y., Kazyak, E., Chen, K.H., Sanchez, A.J., Poli, A., Arruda, E.M., Thouless, M.D., Dasgupta, N.P., 2019. Lithium mechanics: roles of strain rate and temperature and implications for lithium metal batteries. J. Electrochem. Soc. 166 (2), A89.
Lin, D., Liu, Y., Cui, Y., 2017. Reviving the lithium metal anode for high-energy batteries. Nat. Nanotechnol. 12 (3), 194.
Liu, X., Athanasiou, C.E., Padture, N.P., Sheldon, B.W., Gao, H., 2020. A machine learning approach to fracture mechanics problems. Acta Mater. 190, 105–112.
Li, Y., Wang, J., Zhao, F., Bai, B., Nie, G., Nel, A.E., Zhao, Y., 2018. Nanomaterial libraries and model organisms for rapid high-content analysis of nanosafety. Natl. Sci. Rev. 5 (3), 365–388.
Masias, A., Felten, N., Garcia-Mendez, R., Wolfenstine, J., Sakamoto, J., 2019. Elastic, plastic, and creep mechanical properties of lithium metal. J. Mater. Sci. 54 (3), 2585–2600.
Messer, R., Noack, F., 1975. Nuclear magnetic relaxation by self-diffusion in solid lithium: T 1-frequency dependence. Appl. Phys. 6 (1), 79–88.
Meyers, M.A., Armstrong, R.W., Kirchner, H.O., 1999. Mechanics and Materials: Fundamentals and Linkages. Wiley-VCH.
Mozaffar, M., Bostanabad, R., Chen, W., Ehmann, K., Cao, J., Bessa, M.A., 2019. Deep learning predicts path-dependent plasticity. Proc. Natl. Acad. Sci. 116 (52), 26414–26420.
Narayan, S., Anand, L., 2018. A large deformation elastic–viscoplastic model for lithium. Extreme Mech. Lett. 24, 21–29.
Natekin, A., Knoll, A., 2013. Gradient boosting machines, a tutorial. Front. Neurorobot. 7, 21.
Porz, L., Swamy, T., Sheldon, B.W., Rettenwander, D., Frömling, T., Thaman, H.L., Berendts, S., Uecker, R., Chiang, Y.M., 2017. Mechanism of lithium metal penetration through inorganic solid electrolytes. Adv. Energy Mater. 7 (20), 1701003.
Shi, Z., Tsymbalov, E., Dao, M., Suresh, S., Shapeev, A., Li, J., 2019. Deep elastic strain engineering of bandgap through machine learning. Proc. Natl. Acad. Sci. 116 (10), 4117–4122.
Wang, Y., Cheng, Y.T., 2017. A nanoindentation study of the viscoplastic behavior of pure lithium. Scr. Mater. 130, 191–195.
Wang, Z., Li, X., Chen, Y., Pei, K., Mai, Y.W., Zhang, S., Li, J., 2020. Creep-enabled 3D solid-state lithium-metal battery. Chem. 6 (11), 2878–2892.
Wood, K.N., Noked, M., Dasgupta, N.P., 2017. Lithium metal anodes: toward an improved understanding of coupled morphological, electrochemical, and mechanical behavior. ACS Energy Lett. 2 (3), 664–672.
Xu, C., Ahmad, Z., Aryanfar, A., Viswanathan, V., Greer, J.R., 2017. Enhanced strength and temperature dependence of mechanical properties of Li at small scales and its implications for Li metal anodes. Proc. Natl. Acad. Sci. 114 (1), 57–61.
Xu, W., Wang, J., Ding, F., Chen, X., Nasybulin, E., Zhang, Y., Zhang, J.G., 2014. Lithium metal anodes for rechargeable batteries. Energy Environ. Sci. 7 (2), 513–537.
Zhang, W.J., 2011. Structure and performance of LiFePO4 cathode materials: A review. J. Power Sources 196 (6), 2962–2970.
Zhang, X., Wang, Q.J., Harrison, K.L., Roberts, S.A., Harris, S.J., 2020. Pressure-driven interface evolution in solid-state lithium metal batteries. Cell Rep. Phys. Sci. 1 (2), 100012.